



Edge-distributed iron single-atom moiety with efficient “trapping-conversion” for polysulfides driving high-performance of Li-S battery

Fanchao Zhang^a, Zihuan Tang^b, Lirong Zheng^c, Tengfei Zhang^a, Mengyuan Xu^a, Hong Xiao^a, Huifeng Zhuang^a, Pinyu Han^a, Qiuming Gao^{a,*}

^a Key Laboratory of Bio-inspired Smart Interfacial Science and Technology of Ministry of Education, Beijing Advanced Innovation Center for Biomedical Engineering, School of Chemistry, Beihang University, Beijing 100191, PR China

^b The State Key Laboratory of Refractories and Metallurgy, Institute of Advanced Materials and Nanotechnology, Wuhan University of Science and Technology, Wuhan 430081, PR China

^c Beijing Synchrotron Radiation Facility, Institute of High Energy Physics, Chinese Academy of Sciences, Beijing 100049, PR China

ARTICLE INFO

Keywords:

Single-atom sites
Edge-distributed
Li-S battery
Shuttle effect
Trapping-conversion

ABSTRACT

Great efforts are exploring single-atom (SA) sites for tailoring catalytic effects on the sulfur-related redox reaction in Li-S battery, while edge-distributed SA sites lack attention. Herein, we implanted SA iron sites in N-doped porous carbon on CNTs (Fe-NPC@CNTs) to obtain edge-distributed FeN₄ moieties via a polymer inductive strategy. The Fe-NPC@CNTs own enhanced “trapping-conversion” ability for polysulfides. The Li-S battery based on Fe-NPC@CNTs achieves a wonderful capacity of 1004 mAh g⁻¹ at 1 C with long-term cycling stability, where the capacity fading rate is 0.032% per cycle over 1200 cycles. Noteworthy, the cell delivers very large capacities of 3.94/6.12 mAh cm⁻² under high sulfur loadings of 4.50/5.04 mg cm⁻² at 0.5/0.2 C, corresponding to 82.5/82.4% capacity retentions over 100 cycles. Under ultrahigh sulfur loadings (7.8/10.9 mg cm⁻²), the cell exhibits amazing large areal capacities of 7.63/10.76 mAh cm⁻². The edge-distributed SA sites engineering provides a bright blueprint for advanced Li-S battery.

1. Introduction

Lithium-sulfur (Li-S) battery is a highly promising sustainable next-generation battery system, due to its outstanding energy density (2600 Wh kg⁻¹), low cost and environmentally benign nature of sulfur active materials [1,2]. Unfortunately, the practical application of Li-S battery is impeded by several obstacles, such as intrinsic electrical insulation feature of sulfur and its discharging products (Li₂S₂/Li₂S), large volume expansion of active material, and more importantly, the shuttle effects stemming from accumulation and diffusion of soluble lithium polysulfides (LiPSs) in the electrolyte during sulfur-related redox reaction (SROR) process, led to rapid capacity decay, anode passivation and low sulfur utilization in Li-S battery [3–5]. To address aforementioned challenges, majority of works have been done to improve the SROR kinetics and weaken the shuttling effect, including design of nanostructured sulfur host materials, functional separators/interlayers and advanced electrolytes [6–14]. Notably, the

separator modification with advanced catalyst has been considered an effective strategy to enhance the SROR kinetics and remit the LiPSs shuttling effect in Li-S battery. Ideal functional separator can effectively adsorb and restrain the diffusion of LiPSs and hold good transmission of Li-ion. To date, various types of nonpolar carbonaceous materials or polar compounds with high conductivity were developed and used for functional coatings of the separator [7,15]. Nevertheless, the materials are still limited on account of finite physical confinement and chemical adsorption, and they cannot further expedite the SROR kinetics in Li-S battery. Therefore, it is urgent to develop an advanced functional separator with high-efficiency electrocatalyst endowing Li-S battery with rapid SROR conversion and inhibit the shuttling effect of LiPSs.

Recently, single-atom catalysts (SACs) exhibited excellent electrocatalytic activities in various energy conversion systems, benefited by the maximized atomic utilization and regulate electron configuration of the metal sites [16–19]. The SACs were demonstrated to improve the SROR kinetics in Li-S battery and the catalytic efficiency is closely

* Corresponding author.

E-mail address: qmgao@buaa.edu.cn (Q. Gao).

<https://doi.org/10.1016/j.apcatb.2023.122876>

Received 2 April 2023; Received in revised form 24 April 2023; Accepted 10 May 2023

Available online 11 May 2023

0926-3373/© 2023 Elsevier B.V. All rights reserved.

related to the microscopic metal sites and the macroscopic geometry of the catalyst [20–23]. For instance, Han et al. introduced a substrate-strain tuned geometry distortion of Cu-N₂C₂ sites on CNTs to promote the electrons transfer from metal centers to the adsorbed O, thereby enhancing the oxygen reduction reaction (ORR) activity [21]. Liu et al. fabricated Pt SACs with curved interface nature to effectively promote the charge delivery and regulate the local electric field of active moiety, leading to a highly active for hydrogen evolution reaction [22]. Wang et al. constructed N-modified divacancies trapped Fe species which displayed a high ORR activity [23]. Obviously, the maximum exposure and tailor the electronic structure of the metal atoms can markedly improve the catalytic activity of SACs. Unfortunately, the efficiency of SROR is still unsatisfactory over the SACs, owing to the complex 16-electron conversion process including homogeneous and heterogeneous reactions in Li-S battery. Therefore, realizing the high exposure rate of metal active centers is crucial to optimize the catalytic property for SROR. It is worth noting that selecting highly conductive carbon substrates with certain curvature or microscopic bending geometry, would be favorable for precise design of exposed single atom (SA) centers with high activity and stability [24–26]. In this regard, the carbon nanotubes (CNTs) not only exhibit remarkable stability and electronic conductivity, but also possess geometric bended micro-structures, thus can be selected as initial substrates profiting for the distinctive dynamic evolution of active sites based on the service platforms [21,27–29]. On the other hand, the SACs are usually manufactured *via* a pyrolysis strategy, and the metal atoms are extremely easy to form aggregation because of the thermal migration under high temperature; therefore, effective measures must be taken to predisperse the metal ions and reduce the migration energy barrier on the matrix surface during the pyrolysis process.

Herein, a polymer inductive strategy is proposed to fabricate highly exposed edge-distributed SA FeN₄ moieties in the N-doped porous carbon hierarchically anchored on the CNTs (Fe-NPC@CNTs). The Fe-NPC@CNTs have obviously enhanced “trapping-conversion” ability for LiPSs. During the discharge/charge process, the Fe-NPC@CNTs catalyst not only possessed excellent chemical adsorption for LiPSs, but also realized rapid SROR kinetics. Benefiting from the Fe-NPC@CNTs catalyst modified separator, the Li-S battery demonstrated high reversible capacity, superior rate capability and outstanding cycling stability. Notably, even under ultrahigh sulfur loading, the cell achieved a competitive discharge capacity exhibiting the tremendous potential for practical application.

2. Experimental Section/Methods

2.1. Fabrication of Fe-NPC@CNTs

Approximately 50 mg of commercial carbon nanotubes (CNTs) were first dispersed in the Tris-buffer solutions containing 50 mL of ethanol and 30 mL of deionized water and sonication for 1 h. Then, the 0.2 mmol of hemin and 0.6 mL of ammonium hydroxide (28–30 wt%) were added into 20 mL of deionized water under stirring. Subsequently, the hemin solution was dropwise added into the aforementioned CNT/Tris-buffer solution and sonication for 1 h. After that, 80 mg of dopamine was added in the above mixture. After vigorously stirring for 24 h, the precipitates (Hemin-PDA@CNTs) were obtained by centrifuged, washed and dried. Finally, the Fe-NPC@CNTs catalysts were acquired by calcining the resultant precipitates at 700 °C for 5 h under Ar gas. The NPC@CNTs were obtained using a similar fabrication process, except for absences of hemin and ammonium hydroxide.

2.2. Material Characterization

The morphologies of the as-prepared materials were investigated by a field-emission scanning electron microscope (SEM, JEOL, JSM7500) and a transmission electron microscopy (TEM, JEOL 2100 F). The high-

angle annular ark-field scanning transmission electron microscopy (HAADF-STEM) with double-aberration-corrected corrector images and corresponding EDX mapping analyses were obtained on a JEM-ARM300F with an acceleration voltage of 300 kV. X-ray diffraction (XRD) patterns were obtained on a Rigaku D/max2200PC using Cu K_α ($\lambda = 0.15418$ nm) radiation source. The chemical state of materials was surveyed by X-ray photoelectron spectroscopy (XPS, Thermo Scientific, ESCALAB 250 XI). The loading of Fe was measured by inductively coupled plasma optical emission spectrometer (ICP-OES, Agilent 725). The nitrogen adsorption-desorption isotherms were analyzed using Micromeritics ASAP 2010 system at 77 K. Raman spectra were obtained by a Jobin Yvon (Laboratory RAM HR800) using a 633 nm laser as the light source. The static contact angle (CA) was detected using a contact angle meter (JC2000D3M). X-ray absorption fine structure spectra (XAFS) with the acquired X-ray absorption near-edge structure (XANES) and extended X-ray absorption fine structure (EXAFS) were operated at the 1W1B station of Beijing Synchrotron Radiation Facility, P. R. China.

2.3. Fabrication of functional separator

The functional separators were fabricated by a vacuum filtration method. In a typical process, the as-prepared Fe-NPC@CNTs (80 wt%), and polyvinylidene difluoride (PVDF, 20 wt%) were dispersed into dimethyl formamide solvent under sonication procedure to get a homogeneous solution, and then, a vacuum pump filtered out the above solution to coat Fe-NPC@CNTs catalyst on propylene (PP, Celgard-2500) separator. The Fe-NPC@CNTs functional separator was dried thoroughly overnight, and subsequently cut into disks with a diameter of 19 mm. All the reference samples were fabricated by the same method except that the Fe-NPC@CNTs catalysts were replaced by reference samples.

2.4. Electrochemical measurement

The regular sulfur cathodes were prepared by spreading sulfur slurry (60 wt% sulfur, 20 wt% CNTs, 10 wt% acetylene black, and 10 wt% PVDF) onto Al foil collectors, and then vacuum dried at 60 °C for 12 h. The regular sulfur cathode samples were punched into discs with area of about 1 cm² to assemble in CR2032-type coin cells, and the sulfur loading is 1.0–1.5 mg_(s) cm^{−2}. Especially, the nickel foam was used as collector when the sulfur loading was above 4.0 mg_(s) cm^{−2} for the sulfur cathode. It is facile to achieve a thick electrode for the porous metal current collector without delamination from the current collector compared with the traditional Al foil. Moreover, the metal foam current collector can also enhance the energy density of Li-S battery per unit area, owing to the improved low internal contact resistance, unique mechanical property, safety margin, high reaction area, as well as interconnected porous structure accommodated sulfur [30–32]. The electrolyte contains a mixture of 1.0 M bis(trifluoromethane) sulfonamide lithium (LiTFSI) in 1,2-dimethoxyethane (DME) and 1,3-dioxolane (DOL) (1:1 v/v) with 2.0 wt% LiNO₃ additive. The Li-S coin cells were assembled in an Ar-argon-filled glovebox. The Li-S cells were measured by a battery tester (LAND, China) with a voltage range of 1.7–2.7 V. The cells used for cyclic voltammetry (CV) and electrochemical impedance spectroscopy (EIS) were recorded on a CHI660D electrochemical test system. The CV curves were recorded in a voltage potential window of 1.6–2.8 V (vs Li⁺/Li) at a scan rate range of 0.1–0.5 mV s^{−1}. The EIS spectra were recorded in the frequency range of 0.01 Hz–100 kHz.

2.5. Potentiostatic nucleation of Li₂S

For the survey of liquid-solid conversion kinetics, potentiostatic nucleation of Li₂S on different catalyst surfaces was carried out using Li foil anodes and catalyst (Fe-NPC@CNTs or NPC@CNTs) electrodes to assemble the coin-cells. The electrolytes contain 0.25 M Li₂S₈, 1 M

LiTFSI, and 2.0 wt% LiNO₃. The Li-Li₂S₈ cells were discharged galvanostatically at 0.01 mA to 2.10 V, and then kept potentiostatically at 2.09 V for Li₂S to nucleate until the current was lower than 0.01 mA. The nucleation capacity of Li₂S can be calculated by the integral area of the plotted curve through Faraday's Law.

2.6. Density Functional Theory (DFT) Calculation

First-principle calculations (DFT) were performed using the DMol3 code of Material Studio (Accelrys, Inc.) to investigate the geometric structures. The Brillouin zone was a (1 × 1 × 1) area. Monkhorst-Pack mesh of k-points was used for the geometrical optimization, and all-electron DFT energy calculations were utilized for all elements. A double numerical plus polarization (DNP) basis set24 was implemented with a global orbital cut off of 4.0 Å. The Perdew-Burke-Ernzerhof (PBE) generalized gradient function was employed for the exchange correlation energy. Geometries were fully optimized with the convergence criteria for energy, force and displacement less than 10e⁻⁵ Hartree, 0.002 Hartree Å⁻¹ and 0.005 Å, respectively. To further explain the relative reaction trend of Li₂S_n and S₈ species, the Gibbs free energy of each species was calculated as following Eq. (1):

$$\Delta G = \Delta E + \Delta E_{\text{ZPE}} - T\Delta S \quad (1)$$

where ΔE is the reaction energy from the density functional theory calculations. ΔE_{ZPE} and ΔS are the zero point energy difference and entropy between the product and reactant, respectively.

Deformation charge density and electron localization function (ELF) were carried out based on density functional theory (DFT) as implemented in Vienna *ab initio* simulation package (VASP) with exchange-correlation functional of generalized gradient approximation (GGA) of Perdew, Burke, and Ernzerhof (PBE) method. A grid of 3 × 3 × 1 Monkhorst-Pack k-points was used for the structural relaxation. A vacuum layer of 15 Å is adopted in the direction perpendicular to the

monolayer surface to avoid the interactions between periodic slabs. The energy cutoff was set to be 500 eV. The convergence criterion for the energy and maximum force for the optimization were set to 10⁻⁵ eV and 0.05 eV Å⁻¹, respectively.

3. Results and discussion

3.1. Density functional theory calculations for the structure-activity relationship

To determine the structure-activity relationship, theoretical DFT calculations were performed to well unravel the intrinsic activity of highly exposed edge-distributed Fe sites introduced by the NPC@CNTs. Fig. 1a,b shows two typical optimized structural models of Fe-N₄-C and Fe-N₄-edge denoted as in-plane Fe-N₄ and edge-distributed Fe-N₄ sites, respectively. Notably, the optimized edge-distributed Fe-N₄ model has a slightly curved structure with single atom Fe protruding out of the carbon substrate (Fig. S1). In fact, the metal-N₄ site (Me-N₄) with geometry distortion can readily trigger intensive electronic localization and large charge gradient in compare to the square planar Me-N₄, which is believed to improve the catalytic activity in the SROR processes [33, 34]. Fig. 1c,d presents the charge density difference of in-plane and edge-distributed Fe-N₄ sites, respectively. The well electron-accepting ability of the nitrogen atoms induced the charge transfers from Fe atom, and would lead to positive oxidation state of Fe site. Apparently, the edge-distributed Fe-N₄ sites exhibited a charge transfer of -0.209 eV much higher than that of the in-plane Fe-N₄ sites (-0.021 eV) (Table S1), which could induce charge redistribution and weaken the symmetry of Fe-N₄ moieties, favorable for polysulfides adsorption and subsequent reduction process. In addition, the electron localization functions (Fig. 1e,f) further revealed the strong electronic localization of edge-distributed Fe-N₄ moiety coming from the increased electron transfers compared to that of in-plane Fe-N₄ site. Obviously, the high electron transfers of edge-distributed Fe-N₄ moiety implies reduced

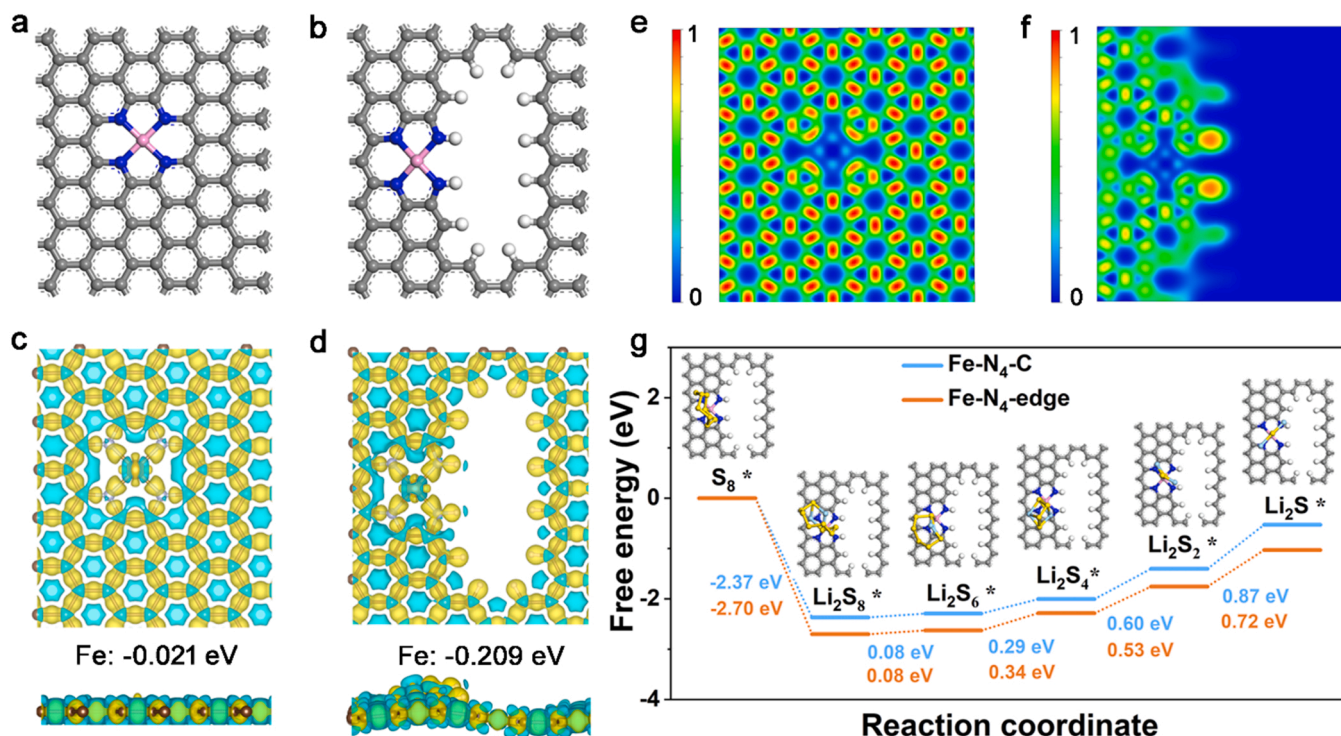


Fig. 1. Theoretical calculations describing the structure-activity relationship. Constructed periodic structure models: (a) in-plane Fe-N₄ and (b) edge-distributed Fe-N₄ structures. The charge density difference of (c) in-plane Fe-N₄ and (d) edge-distributed Fe-N₄ sites. The electron localization function maps of (e) in-plane Fe-N₄ and (f) edge-distributed Fe-N₄ sites. And (g) Gibbs free energy diagrams for the stepwise sulfur species reduction on in-plane Fe-N₄ and edge-distributed Fe-N₄ sites. Insets show the optimized geometrical structures.

outer orbital electrons of Fe atoms which are favorable for forming $S_x \cdots Fe-N$ bonds with the polysulfides, thus enhancing the chemical affinity and reducing reaction energy barrier [35,36].

To well disclose the excellent catalytic effect of edge-distributed $Fe-N_4$ moiety for the conversion of polysulfides, the Gibbs free energy diagrams with the optimized geometrical structures from S_8 to Li_2S are illustrated in Fig. 1 g and S2. The solid-solid reaction process from Li_2S_2 to Li_2S presented a larger thermodynamic energy barrier than those of the other steps on both in-plane and edge-distributed $Fe-N_4$ models, indicating that it is the rate-determine step in sulfur reduction reaction process. The edge-distributed $Fe-N_4$ surface displayed a lower energy barrier of 0.72 eV than that of the in-plane $Fe-N_4$ surface (0.87 eV) in the

rate-determine step, well demonstrating the faster redox kinetics. Moreover, the liquid-solid conversion from Li_2S_4 to Li_2S_2 on edge-distributed $Fe-N_4$ surface also showed a lower energy barrier of 0.53 eV than that of in-plane $Fe-N_4$ surface (0.60 eV), further indicating the enhanced conversion of LiPSs to avoid the accumulation in electrolyte, contributing to prevent the LiPSs shuttling effect. Thus, the above results well expounded the excellent catalytic improvement over the edge-distributed $Fe-N_4$ moiety in the SROR process.

3.2. Synthesis and Microstructure of Fe-NPC@CNTs

The synthesis of Fe-NPC@CNTs is carried out by a typical polymer

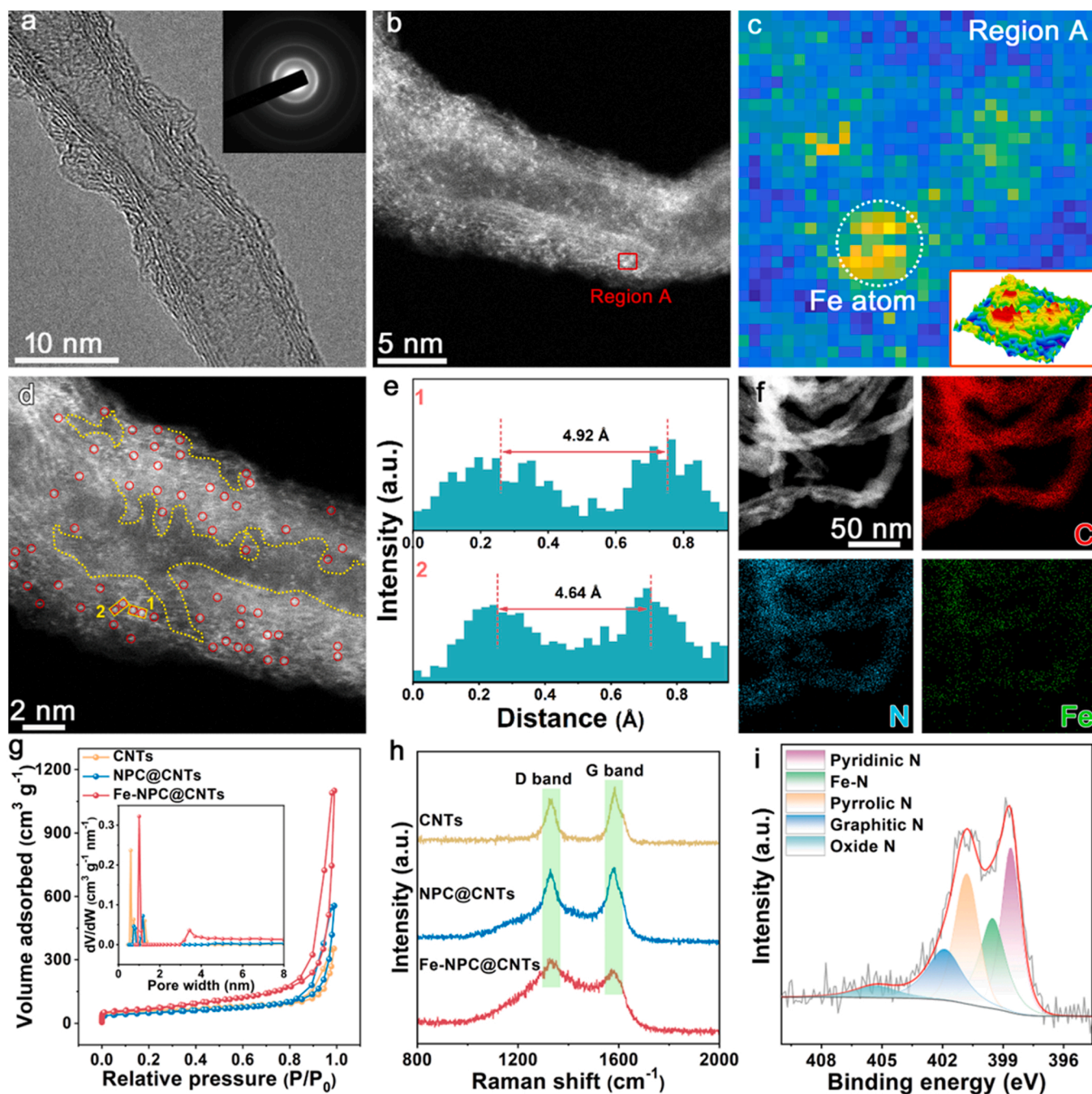


Fig. 2. Preparation and characterization of Fe-NPC@CNTs. (a) TEM image with the inset showing the SAED pattern. (b) HAADF-STEM image. (c) The heat maps in region A of Fig. 2b. (insets show corresponding the three-dimensional mapping in region A). (d) HAADF-STEM image with atomic identification. (e) Intensity profile along the region 1 and 2 in d. (f) HAADF-STEM and corresponding EDX mappings of C, N, and Fe elements for Fe-NPC@CNTs. (g) N_2 adsorption/desorption isotherms and corresponding pore size distributions for samples. (h) Raman spectra of different samples. And (i) high-resolution N 1s XPS spectrum of Fe-NPC@CNTs.

inductive-pyrolysis strategy. Firstly, the commercial CNTs were dispersed in Tris-buffer solution, and then dopamine (with $-NH_2$) polymerized and induced hemin molecules (with $-COOH$) predispersion on the surface of CNTs substrate, followed by pyrolysis to obtain atomically dispersed iron sites in the N-doped porous carbon hierarchically anchored on the CNTs (named as Fe-NPC@CNTs). Obviously, the Fe-NPC@CNTs owns well-defined hierarchical cross-stacking nanotube structure, where the highly graphitized CNTs were coated with N-doped porous amorphous carbon with a rough and curved structure (Fig. 2a and S3). High-resolution transmission electron microscopy (HR-TEM) confirmed that no distinctly metal particles can be observed in the Fe-NPC@CNTs sample, indicating the iron element is possibly atomically dispersed in the sample. Meanwhile, the selected-area electron diffraction (SAED) (Fig. 2a, inset) only displayed the crystallized sp^2 -hybridized characteristic of carbon, which is consistent with the highly graphitized CNTs.

To further reveal the microstructure of Fe-NPC@CNTs, HAADF-STEM was used to reveal the hierarchical structure (Fig. S3d). Obviously, there are more atomic bright points on the edge (amorphous layer) than on the inside. The local morphologies of Fe-NPC@CNTs also revealed that the dense Fe atoms are distributed in overall surface of carbon substrates (Fig. 2b). Furthermore, the heat maps (Fig. 2c) and three-dimensional mapping (inset of Fig. 2c, low right) in region A (Fig. S4) of Fig. 2b well verified the formation of isolated Fe atoms. As shown in Fig. 2d, the isolate Fe atoms marked by red circles are main around defects edge (dark color marked by yellow lines in Fig. 2d). Moreover, the corresponding intensity profiles of along 1 and 2 of Fig. 2d revealed the distances of Fe atoms are 4.92 and 4.64 Å, respectively (Fig. 2e), well demonstrating that no Fe-Fe chemical bonds are formed in Fe-NPC@CNTs. Clearly, the formation of polymer cladding is crucial to restrain the thermal migration of Fe atoms transforming into clusters or nanoparticles under high-temperature pyrolysis due to the reduced surface energy [37,38]. The dopamine with amino functional groups may interact with carboxy group of hemin molecules under weak alkaline solution during polymerization, which would lead to predispersion of the metal precursors. In addition, the HAADF-STEM and EDX spectroscopy elemental mappings revealed that the Fe, N and C elements (Fig. 2f) exist homogeneously throughout the CNTs substrate. The content of Fe is 1.86 wt% in Fe-NPC@CNTs determined by ICP-OES.

The specific surface area and pore size distribution were surveyed by N_2 adsorption/desorption isotherms (Fig. 2g and Table S2). The Fe-NPC@CNTs displayed a higher Brunauer-Emmett-Teller (BET) surface area of $256 \text{ m}^2 \text{ g}^{-1}$ than those of NPC@CNTs ($174 \text{ m}^2 \text{ g}^{-1}$) and CNTs ($214 \text{ m}^2 \text{ g}^{-1}$). The pretty high specific BET surface area of Fe-NPC@CNTs would lead to luxuriant accessible active sites, which could afford to catalytic conversion of SROR [39,40]. Notably, the variation of micropore ($< 2 \text{ nm}$) and creation of mesoporous (3.4 nm) signified that both Fe sites and edge defects are successfully rooted in the surface of Fe-NPC@CNTs (inset of Fig. 2g). Obviously, the Fe-NPC@CNTs exhibited a high pore volume of $1.70 \text{ cm}^3 \text{ g}^{-1}$ which is about twice of NPC@CNTs ($0.86 \text{ cm}^3 \text{ g}^{-1}$) and triple of CNTs ($0.55 \text{ cm}^3 \text{ g}^{-1}$). XRD pattern of Fe-NPC@CNTs displayed two weak broad peaks corresponding to the characteristic peak of sp^2 -hybridized carbon, similar to that of NPC@CNTs (Fig. S5a) [18]. The diffraction peaks of metallic nanoparticles or oxides were not visible for Fe-NPC@CNTs. The Fe-NPC@CNTs possessed a larger full-width at half-maximum of peak at around 44° than the NPC@CNTs sample, implying the increased defects in Fe-NPC@CNTs (Fig. S5b) [33,35]. Raman spectra were employed to survey structures of the catalysts (Fig. 2h). Two distinct peaks around at 1580 and 1338 cm^{-1} of Fe-NPC@CNTs were observed, which are corresponding to graphitic carbon-related G-band and defect-related D-band, respectively. Predictably, the high I_D/I_G ratio signified that there are more defects caused by the Fe atoms for Fe-NPC@CNTs (Fig. 2h) [34,35,37,39]. XPS was employed to investigate the chemical state of Fe-NPC@CNTs. High-resolution N 1s XPS spectra of Fe-NPC@CNTs revealed five types of nitrogen, corresponding to oxide N

(405.3 eV), graphitic N (401.8 eV), pyrrolic N (400.8 eV), Fe-N (399.5 eV) and pyridinic N (398.6 eV) (Fig. 2i) [39]. The affluent Fe-N sites may afford to catalytic SROR conversion and accelerate the kinetics. High-resolution Fe 2p XPS spectrum indicated that Fe 2p is between Fe^{2+} (709.6 eV) and Fe^{3+} (711.6 eV), signifying that the valence of Fe is between +2 and +3 (Fig. S6) [40].

XAFS was employed to deeply unravel the electronic and coordination structure of Fe atoms in Fe-NPC@CNTs with the references of iron phthalocyanine (FePc), Fe_2O_3 and Fe foil. Fig. 3a shows the Fe K-edge XANES profiles of all samples. The near-edge absorption energy (E_0) of Fe-NPC@CNTs is higher than that of the Fe foil, implying the positive electric charge state of Fe atoms in Fe-NPC@CNTs. The pre-edge peak at around 7113 eV may be attributed to the characteristic fingerprint ($1s \rightarrow 4p_z$ shakedown transition) of FePc with high D_{4h} symmetric configuration [41]. Notably, the Fe-NPC@CNTs also showed the similar edge peak with that of FePc, but the weakening pre-edge feature indicates the fine-tuning coordination environment of Fe atoms. To well identify the valence state of Fe atoms, the first-derivatives of XANES are shown in Fig. 3b. The Fe-NPC@CNTs exhibited the highest first-derivative of absorption threshold at 7125.7 eV in XANES, which is situated between Fe foil (7120.6 eV) and Fe_2O_3 (7126.7 eV). The oxidation state of Fe in Fe-NPC@CNTs was determined to be +2.5 on the basis of linear relationship between E_0 and oxidation state (Fig. 3c). Obviously, the high valence state of Fe in Fe-NPC@CNTs is correspondence with the significantly reduced outer orbital electrons of Fe atom [35], which may be on account of the enhanced interaction between Fe species with substrate, leading to intensified electronic transfer from Fe atoms of edge-distributed Fe-N₄ moiety to carbon substrate, well consistent with the DFT results (Fig. 1). The Fe moiety with high valence state is deemed to facilitate the adsorption and SROR conversion [39,40]. Fourier transform extended X-ray absorption fine structure (FT-EXAFS) spectrum of Fe R space in Fe-NPC@CNTs exhibited an apparent peak located at about 1.41 Å, which is associated with Fe-N contribution at the first shell (Fig. 3d). The faint shift of the peak in Fe-NPC@CNTs indicated the different local electronic environment from FePc. No Fe-O (1.53 Å) and Fe-Fe (2.22 Å) scattering paths could be observed in Fe-NPC@CNTs compared with the references of Fe_2O_3 and Fe foil. Moreover, wavelet transform (WT) of the k^3 -weighted EXAFS spectrum in Fe-NPC@CNTs reflected the only one intensity at around 3.2 Å^{-1} , corresponding to the Fe-light atoms bonding, which is distinct from Fe foil and Fe_2O_3 , well indicating atomically dispersed states of Fe atoms in Fe-NPC@CNTs (Fig. 3e). The best K-edge EXAFS analysis clearly exhibited the only Fe-N first shell coordination of Fe-NPC@CNTs in R (Fig. 3f) and K (Fig. 3g) spaces. The fitting result indicated that the geometry of Fe site of Fe-NPC@CNTs is a configuration with four nitrogen atoms at 1.975 Å (Fig. 3f and Table S3), which slightly shorter than Fe-N distances in Fe-N₄ and FePc (1.998 Å) at the first shell, further demonstrating the stronger Fe-N coordination for Fe-NPC@CNTs because of the intensive charge transfer in edge-distributed iron SA moieties.

3.3. Property of Fe-NPC@CNTs Catalyst

The Fe-NPC@CNTs catalyst modified separator was prepared by a vacuum filtration method with coating the functional catalysts onto the surface of pristine separator. Compared with the pristine separator (Fig. S7a) with hundreds of nanometer scale slits, the Fe-NPC@CNTs catalyst modified separator exhibited a tight functional catalyst coating (Fig. S7b) and hierarchical pore structure (Fig. S7c), which would be beneficial for the transport of Li-ions. Meanwhile, the three-dimensional interconnected Fe-NPC@CNTs catalyst networks (Fig. S7d) can effectively catalyze the SROR conversion and restrain the diffusion of LiPSs as a powerful barrier. The thickness of functional catalyst coating is about $21 \mu\text{m}$ (Fig. S7e), which was made of carbon nanotubes interwoven and stacked. The mass loading of Fe-NPC@CNTs on the separator is about 0.3 mg cm^{-2} , which is appropriate compared with those of the reports [15,36]. The contact angle tests are exhibited in

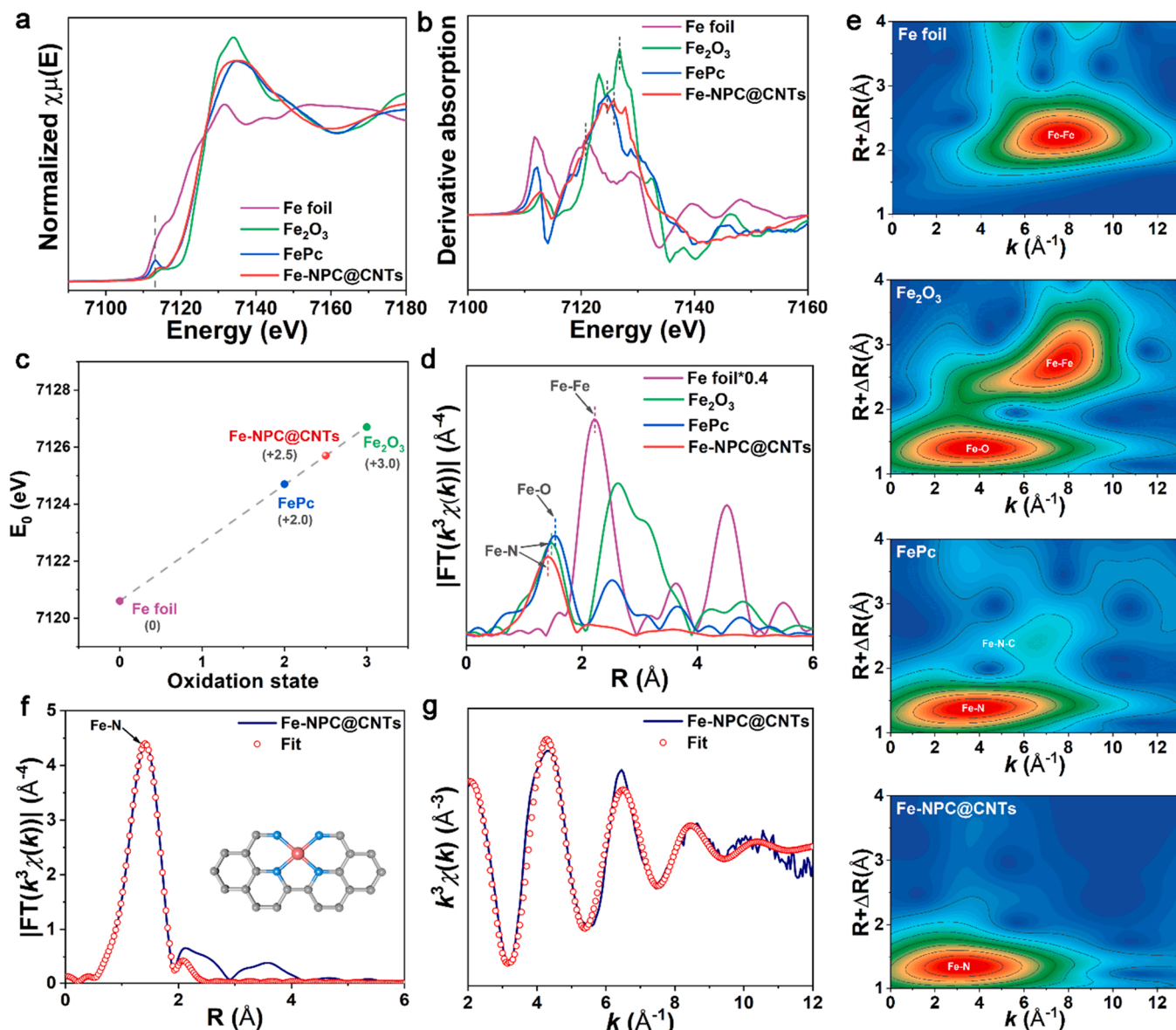


Fig. 3. XAFS characterizations of the Fe-NPC@CNTs. (a) Fe K-edge XANES spectra and (b) first derivatives of XANES of Fe K-edges for Fe-NPC@CNTs, FePc, Fe_2O_3 and Fe foil. (c) Fe oxidation states for Fe-NPC@CNTs and reference samples. (d) FT curves of Fe K-edge EXAFS spectra (R space plots) and (e) WT-EXAFS plots for Fe-NPC@CNTs and reference samples. And fitting curves of the Fe K-edge FT EXAFS spectra in (f) R and (g) K spaces for the Fe-NPC@CNTs (inset in f: the atomic structure model of Fe-NPC@CNTs).

Fig. S7f,g. The electrolyte solution contact angle for pristine PP separator was about 38° . In sharp contrast to pristine PP separator, the Fe-NPC@CNTs modified separator displayed rather small contact angle of 11° , delivering a good wettability to electrolyte solution, which verified an excellent accessibility of the active sites in Fe-NPC@CNTs. In addition, the Fe-NPC@CNTs catalyst coating also revealed the reliable mechanical property (**Fig. S7h-k**), which would contribute to the stability for continuous catalytic conversion of LiPSs during long-term cycles.

The performance of Li-ion diffusion for the Li-S cells with different functional separators were surveyed by cyclic voltammetry (CV) at different scan rates from 0.2 to 0.5 mV s^{-1} (**Fig. S8a-c**). The peak currents for reduction (A and B) and oxidation (C) reactions appeared a linear correlation with the square root of sweeping rates (**Fig. S8d-f**), demonstrating a typical diffusion-limited process. Thus, the Li-ion diffusion ability can be well elucidated by the Randles-Sevcik equation (**Eq. S1**) [34,40]. Impressively, compared with the cells based on NPC@CNTs (0.96, 1.68 and 1.87) and PP (0.81, 1.18 and 1.65) modified

separators, the Li-S battery with Fe-NPC@CNTs modified separator delivered the highest slopes at peaks A, B and C, corresponding to the values of 1.46, 2.23 and 3.15, respectively (**Fig. S8d-f**), indicating the fast electrochemical kinetics arising from the high Li-ion conductivity of Fe-NPC@CNTs functional separator, which would afford to rapid SROR conversion and improve the rate performance.

To verify the excellent adsorbing effect of Fe-NPC@CNTs modified separator for LiPSs, the visualized adsorption experiments were performed. In sharp contrast to the NPC@CNTs and CNTs, the Fe-NPC@CNTs showed a salient ability of decoloration for the blank solution (Li_2S_6) after 8 h dipping (inset of **Fig. 4a**). Moreover, the UV-vis spectroscopy further exhibited the lowest absorbance intensity of the supernatant solution for Fe-NPC@CNTs after adsorption experiments, indicating the strongest chemical affinity (**Fig. 4a**). To well elucidate mechanism of the adsorption, the recovered Fe-NPC@CNTs/ Li_2S_6 precipitate was investigated by XPS. There was an apparent top-shift in high-resolution Fe 2p XPS spectra of Fe-NVNTs/ Li_2S_6 sample compared with the Fe-NPC@CNTs before adsorption experiments (**Fig. 4b**), which

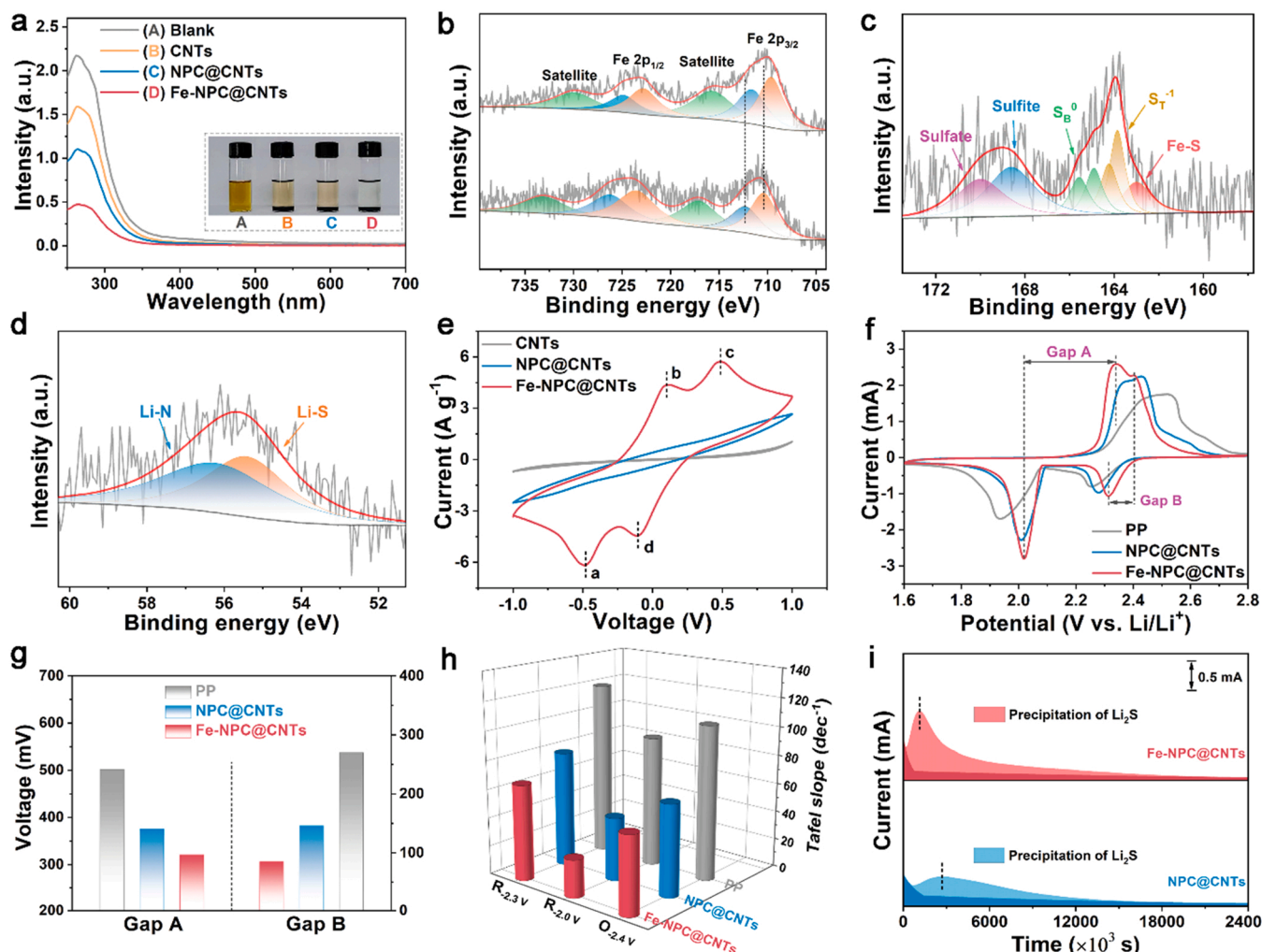


Fig. 4. Adsorption performance test and electrochemical reaction kinetics measurements. (a) UV-vis adsorption spectra photograph (inset) of Li_2S_6 solution before and after adsorption by various materials. (b) Co 2p XPS spectra of Fe-NPC@CNTs before and after adsorption of polysulfides. XPS profiles of (c) S 2p and (d) Li 1s peaks for Fe-NPC@CNTs after adsorption of polysulfides. (e) CV curves of Li_2S_6 symmetrical cells with the CNTs, NPC@CNTs and Fe-NPC@CNTs electrodes. (f) CV curves of Li-S cells based on Fe-NPC@CNTs and reference samples. (g) Corresponding to potential gaps of oxidation and reduction peaks for the CV curves of Li-S cells. (h) Comparison of Tafel slopes for conversion process of polysulfides in CV curves. And (i) potentiostatic nucleation profiles of Li_2S with NPC@CNTs and Fe-NPC@CNTs.

can be attributed to the enhanced electronegativity arising from strong chemical interaction between Fe in Fe-NPC@CNTs and S atoms in LiPSs. Notably, the high-resolution S 2p spectrum further revealed a peak of 163.0 eV which is attributed to the Fe-S chemical bond (Fig. 4c), indicating the strong chemical strong trapping capability arising from formation of $\text{S}_x \cdots \text{Fe-N}$ bond in highly exposed edge-distributed Fe- N_4 moiety [34,39]. Meanwhile, two pairs of peaks located at 163.9/164.2 eV and 164.9/165.6 eV were observed, which are belonging to the terminal sulfur (S_T^-) and bridging sulfur (S_B^0), respectively. Specially, two obvious peaks located at 168.6 and 170.0 eV attributed to sulfite and sulfate species were found, which are associated with the strong interaction between Fe-NPC@CNTs and LiPSs [34]. Moreover, the Li 1s spectrum of Fe-NPC@CNTs/ Li_2S_6 can be principally deconvoluted into two peaks of 55.4 and 56.2 eV, corresponding to the Li-S and Li-N chemical bonds, respectively (Fig. 4d), which further displaying the strong trapping capability for polysulfides [39].

To further evaluate the electrocatalytic performance of Fe-NPC@CNTs, the Li_2S_6 symmetric cells were performed by using Li_2S_6 -containing (0.25 mol L^{-1}) electrolyte. Fig. 4e exhibits the CV curves of symmetric cells under voltage from -1.0 – 1.0 V. The Fe-NPC@CNTs electrode exhibited two pairs of apparent reversible redox peaks (a, b, c and d) while no obvious redox behaviors could be observed in the CV

curves of NPC@CNTs and CNTs. The reduction peaks at -0.48 (a) and -0.10 V (d) are associated with reversible transformation of LiPSs to Li_2S and S_8 to LiPSs, while the oxidation peaks at 0.10 (b) and 0.48 V (c) correspond to the reversible formations of LiPSs and S_8 , respectively [5, 19,40]. The prominent redox behaviors of Fe-NPC@CNTs demonstrated the outstanding catalytic ability for the sulfur redox conversion in terms of complex homogeneous and heterogeneous reactions in the electrolyte, which can effectively accelerate the LiPSs reduction and Li_2S decomposition. Moreover, the peak currents of Fe-NPC@CNTs were always higher than those of NPC@CNTs and CNTs, further indicating the high electrocatalytic activity of Fe-NPC@CNTs.

To in-depth insight into the superior catalytic capability of Fe-NPC@CNTs for SROR processes, the CV measurement of Li-S cell with Fe-NPC@CNTs was performed under the scan rate of 0.1 mV s^{-1} . Fig. 4f shows the CV plots of Li-S cell with different functional separators. The positions and horizontal shifts of anodic and cathodic peaks in the CV curve could well disclose the reaction kinetics [34]. The Fe-NPC@CNTs cell displayed a smaller anodic peak voltage and higher cathodic peak voltages than those of cells based on NPC@CNTs and PP. Moreover, the cell with Fe-NPC@CNTs modified separator possessed the smallest peak potential gap (Gap A and Gap B) (Fig. 4g), indicating the fast SROR kinetics and high reversible performance for Li-S cell with

Fe-NPC@CNTs functional separator. To accurately elucidate the catalytic activity of Fe-NPC@CNTs, the Tafel slopes derived from CV curves are illustrate in Fig. S9. In fact, the cathodic peaks at about 2.3 V (corresponding to $R_{2.3}$ V) and 2.0 V (corresponding to $R_{2.0}$ V) represent the reduction processes of S_8 to LiPSs and LiPSs to Li_2S , respectively, while the anodic peak at around 2.4 V (corresponding to $O_{2.4}$ V) denotes the oxidation reservation back to S_8 . Obviously, the Fe-NPC@CNTs exhibited the lowest Tafel slopes in the oxidation (54.7 dec^{-1} for $O_{2.4}$ V) and

reduction (66.8 dec^{-1} for $R_{2.3}$ V and 26.5 dec^{-1} for $R_{2.0}$ V) processes (Fig. 4 h and Fig. S9), indicating the continuable excellent electrocatalytic activities of Fe-NPC@CNTs at the overall reversible reaction process. Especially, the Fe-NPC@CNTs catalyst displayed an outstanding advantage for the reversible transformation from LiPSs to Li_2S (corresponding to $R_{2.0}$ V, liquid-solid conversion) (Fig. 4 h), which would lead to high reversible capacity and glorious rate performance.

It is worth mentioning that the conversion capacity from LiPSs to

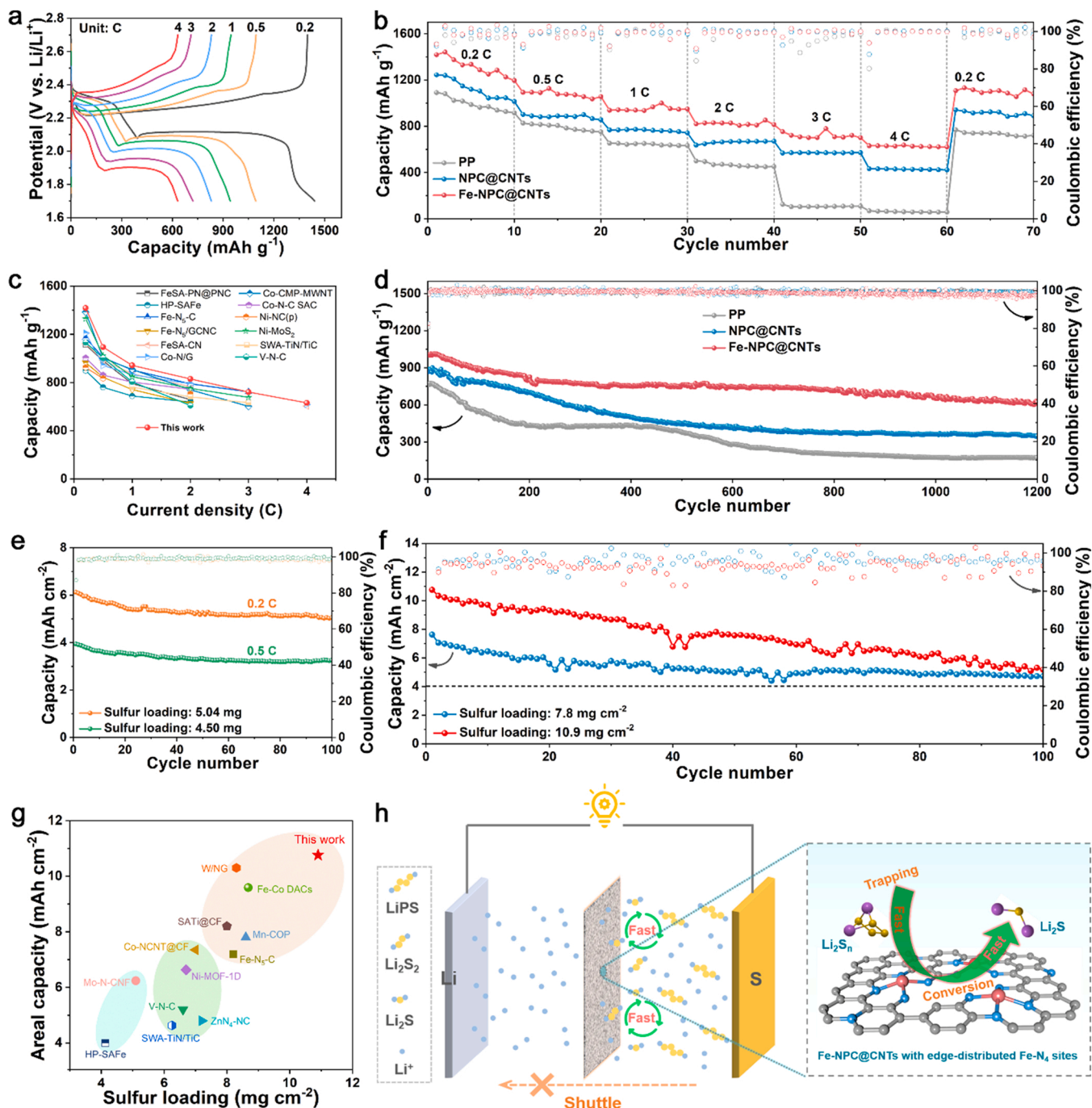


Fig. 5. Electrochemical performance of Li-S batteries. (a) Galvanostatic charge-discharge curves at various current densities for Fe-NPC@CNTs. (b) Rate performance at various current densities. (c) Comparison of the rate performance of Fe-NPC@CNTs with the reported SACs-based Li-S batteries. (d) Cycle performance of Li-S batteries at 1 C. (e) Cycle performances of Fe-NPC@CNTs-based Li-S batteries with high sulfur loading at 0.2 C and 0.5 C, respectively. (f) Cycle performances of Fe-NPC@CNTs-based Li-S battery with different sulfur loadings at 0.1 C (the E/S ratios are about 10.3 and 7.4 $\mu\text{L mg}^{-1}$ corresponding to the sulfur loadings of 7.8 and 10.9 mg cm^{-2} , respectively). (g) Comparison of areal capacity and sulfur loading of Fe-NPC@CNTs-based Li-S battery with previously reported SAC-based materials. And (h) schematic illustrations of Fe-NPC@CNTs-enabled ultrafast conversion kinetics of polysulfides based on efficient “trapping-conversion” mechanism of edge-distributed Fe-N₄ moieties.

Li₂S contributes three quarters of the total discharge capacity. Therefore, the liquid-solid conversion kinetics were further evaluated by the Li₂S nucleation/deposition experiments and are illustrated in Fig. 4i. As expected, the Fe-NPC@CNTs electrode demonstrated an earlier responsivity and a higher capacity (199.7 mAh g⁻¹) of Li₂S nucleation than that of the NPC@CNTs (121.6 mAh g⁻¹) electrode, suggesting that the Fe-NPC@CNTs with edge-distributed Fe-N₄ sites can effectively reduce energy barrier of Li₂S nucleation and rapid SROR kinetics. In addition, the activation energy (E_a) can also assess the redox kinetics of the critical step from LiPSs to Li₂S. Fig. S10a,b showed the CV curves with vary temperature under a scanning rate of 0.2 mV s⁻¹. Based on the relationship between peak current and absolute temperature (Fig. S10c, d), the E_a could be obtained using the Arrhenius equation (Eq. S2) [42]. Obviously, the Fe-NPC@CNTs showed a lower activation energy corresponding to 8.14 kJ mol⁻¹ than the NPC@CNTs (9.03 kJ mol⁻¹), indicating the superior catalytic activity. The Fe-NPC@CNTs with highly exposed edge-distributed Fe-N₄ moiety could not only promote the adsorption of LiPSs by the formation of chemical bond, but also reduced the energy barrier of reversible conversion of polysulfides, specially, enhanced the nucleation of Li₂S, vastly accelerated the redox kinetics, thus inhibited the shuttle effect and acquired a high sulfur utilization.

Electrochemical impedance spectroscopy (EIS) of Li-S cells was performed to investigate the charge transfer ability. The Randles-equivalent circuit fit EIS of the fresh Li-S cells are shown in Fig. S11, and the R_{ct} denotes charge transfer resistance [43]. The Fe-NPC@CNTs based cell displayed a smaller R_{ct} of 21.1 Ω than those of PP (66.0 Ω) and NPC@CNTs (65.7 Ω) based cells, well demonstrating that the Fe-NPC@CNTs endow Li-S battery with preferable charge transfer kinetics, and would promote the reversible conversion reaction of sulfur species.

3.4. Advanced Li-S Battery Based on Fe-NPC@CNTs Catalyst

The galvanostatic charge-discharge profiles of the Li-S cells with Fe-NPC@CNTs modified separator is illustrated in Fig. 5a. The cell with Fe-NPC@CNTs modified separator delivered high discharge capacity of 1418 mAh g⁻¹ and sulfur utilization up to 84.7% at 0.2 C (1 C = 1675 mA g⁻¹) when compared to those of NPC@CNTs (1244 mAh g⁻¹, 74.3%) and PP (1090 mAh g⁻¹, 65.1%). The Fe-NPC@CNTs based Li-S battery in such high discharge capacity and sulfur utilization implied the outstanding kinetics of conversion reactions for polysulfides. Notably, the of Fe-NPC@CNTs based Li-S cell displayed a smaller potential difference (ΔE) of about 145 mV at 0.2 C than those of cells based on NPC@CNTs (160 mV) and PP (175 mV) separators (Fig. S12a), well demonstrating the significantly reduced the barrier of conversion reactions for polysulfides. Obviously, the cell with Fe-NPC@CNTs modified separator all showed small polarization potential under vary current density, especially, the Fe-NPC@CNTs exhibited obvious superiority for reduce the polarization at higher current densities of from 2 to 4 C (Fig. S12). In addition, the Li-S cell with Fe-NPC@CNTs modified separator exhibited excellent rate performances (corresponding to 1094, 942, 830, 721 and 631 mAh g⁻¹ at 0.5, 1.0, 2.0, 3.0 and 4.0 C, respectively), which are superior to the NPC@CNTs and PP (Fig. 5b and S13). Moreover, the Li-S cell with Fe-NPC@CNTs modified separator showed a better returned capacity (1107 mAh g⁻¹) than NPC@CNTs (941 mAh g⁻¹) and PP (769 mAh g⁻¹) based cells at 0.2 C, indicating the great kinetic reversibility of Li-S cell because of the superior catalytic performance of Fe-NPC@CNTs catalysts with edge-distributed Fe-N₄ species. To better reveal the advantage of the cell with Fe-NPC@CNTs modified separator, the comparison of Fe-NPC@CNTs with reported state-of-the-art SACs materials were illustrated in Fig. 5c [19,39,40,44–51]. Obviously, the Li-S batteries with Fe-NPC@CNTs modified separator showed a competitive rate capability.

To further evaluate the cycling stability of cells, the charge/discharge tests of different Li-S cells with a current density of 0.5 C are illustrated in Fig. S14a. The cells with NPC@CNTs and PP configurations

showed the initial capacities of 960 and 800 mAh g⁻¹, respectively, and corresponding to the low capacity retentions (66.5% and 48.8%) and fast capacity decay per cycle (0.067% and 0.102%) after 500 cycles. In contrast, the Fe-NPC@CNTs based Li-S battery delivered a high reversible capacity of 1098 mAh g⁻¹ and an admirable capacity retentive up to about 74%, corresponding to 0.053% decay per cycle after 500 cycles (Fig. S14b). The high reversible capacity and capacity retention of Li-S cell with Fe-NPC@CNTs modified separator further demonstrated the excellent cycling stability, high sulfur utilization and rapid SROR kinetics profited from the everlasting catalytic activities of the Fe-NPC@CNTs. To well evaluate the excellent performance for suppressing the LiPSs shuttling effect of Fe-NPC@CNTs, the morphologies of Li anodes of Li-S batteries before and after cycles are presented in Fig. S15. Compared with the pristine Li anode (Fig. S15a), the cycled Li surface with pristine PP was distinctly corrosive and its large cracks morphology was uneven (Fig. S15b). By contrast, the Li surface of Li-S battery with Fe-NPC@CNTs functional separator was flat and uniform without bulky aggregation (Fig. S15c). As a result, the Fe-NPC@CNTs can effectively suppress the LiPSs diffusion to Li anode to avoid the irregular growth of Li dendrite.

To further evaluated the long-term cycle performance of Li-S cell with Fe-NPC@CNTs modified separator, the cyclic stability tests of cell were performed at 1 C (Fig. 5d). As expected, the Li-S cell with Fe-NPC@CNTs modified separator delivered a high initial capacity of 1004 mAh g⁻¹, which outclasses those of cells based on NPC@CNTs (868 mAh g⁻¹) and PP (767 mAh g⁻¹). More significantly, the cell based on Fe-NPC@CNTs owned a pretty low capacity fading rate of only 0.032% per cycle under 1200 cycles, while the cells based on NPC@CNTs and PP are 0.050% and 0.065%, respectively. Obviously, the cell with Fe-NPC@CNTs modified separator demonstrated admirable capacitive property and cycling stability, which would be profited from the enhanced chemical trapping of LiPSs and excellent electrocatalytic activity of Fe-NPC@CNTs with luxuriant edge-distributed Fe-N₄ moieties.

To fully assess the feasibility of Fe-NPC@CNTs functional separator for the practical application of Li-S batteries, the high sulfur loading cathode and low electrolyte/sulfur (E/S) ratio are crucial to acquire high-energy density [26]. Impressively, the Li-S battery with Fe-NPC@CNTs functional separator showed a high initial capacity of 3.94 mAh cm⁻² (corresponding to 875 mAh g⁻¹) at a high current density of 0.5 C and a high retention rate of 82.5% over 100 cycles (Fig. 5e and S16) at a high sulfur loading of 4.50 mg cm⁻² with E/S ratio of 13.3 μ L mg⁻¹. When the sulfur loadings were increased to 5.04 mg cm⁻² with E/S ratio of 11.9 μ L mg⁻¹, the Li-S cell based on Fe-NPC@CNTs presented an outstanding areal capacity of 6.12 mAh cm⁻² (corresponding to 1214 mAh g⁻¹) at 0.2 C and a competitive retention capacity of 5.04 mAh cm⁻² after 100 cycles, corresponding to a high retention rate of 82.4% (Fig. 5e and S16). In addition, the cycling performance at 0.1 C of Li-S cells based on Fe-NPC@CNTs catalysts with various sulfur loading is presented in Fig. 5f. The Li-S cells based on Fe-NPC@CNTs catalysts delivered favorable areal capacities of 7.63 and 10.76 mAh cm⁻², corresponding to the high sulfur loadings of 7.8 and 10.9 mg cm⁻² and with low E/S ratios of 10.3 and 7.4 μ L mg⁻¹, respectively. After intense 100 cycles, the Li-S cells still appeared superior retained capacities of 4.72 and 5.18 mAh cm⁻², which are superior to that of a typical commercialized Li-ion battery (4 mAh cm⁻²). The high areal capacity and ultrahigh sulfur loading of Li-S cell based on Fe-NPC@CNTs is comparable to state-of-the-art SACs-based Li-S cells (Fig. 5g) [39,40,50–59]. As a demonstration, Fig. S17 shows that single Li-S cell can drive electronic hygrometer thermometer successfully, demonstrating the potential for practical application. Obviously, the outstanding electrochemical performance of Li-S battery with high sulfur loading fully demonstrates the effectiveness of Fe-NPC@CNTs with edge-distributed Fe-N₄ moiety. Thus, we well confirm that the Fe-NPC@CNTs with highly exposed edge-distributed Fe-N₄ moiety can not only intensify the anchoring ability to LiPSs, but also accelerate the

reversible conversion of polysulfides, thereby realized well inhibited LiPSs shuttling by outstanding “trapping-conversion” mechanism of exposed edge-distributed Fe-N₄ sites, and lead to the high sulfur utilization (Fig. 5 h).

4. Conclusions

In summary, we developed a novel kind of Fe-NPC@CNTs SAC with highly exposed edge-distributed Fe-N₄ moiety for the advanced Li-S battery. Importantly, the edge-distributed Fe-N₄ sites can effectively facilitate charge transfers and induce charge redistribution, which can reach an enhanced LiPSs chemical trapping capacity, and expedite reversible conversion of polysulfides. The ultrafast SROR kinetics on Fe-NPC@CNTs SAC well inhibits the LiPSs shuttle effect and achieves a high sulfur utilization. The Li-S battery employing Fe-NPC@CNTs demonstrates high reversible capacity, superior rate capability and outstanding cycling stability. Even under a high sulfur loading, the cell achieves competitive discharge capacity excellently exhibiting the tremendous potential for practical application. This work well confirms that the precise tailoring of interfacial structures of metal atoms can enable enhanced redox kinetics of Li-S chemistry and establish accurate structure-property-function relationships, and have important implications for the designed advanced catalysts for metal-sulfur batteries.

CRedit authorship contribution statement

F.-C.Z., Conceptualization, Formal analysis, Methodology, Writing - Original Draft; Z.-H.T., Formal analysis, Methodology; L.-R.Z., Formal analysis, Methodology, Software; T.-F.Z., Formal analysis; M.-Y.X., Formal analysis; H. X., Formal analysis; H.-F. Z., Formal analysis; P.-Y. H., Formal analysis; And Q.-M.G., Conceptualization, Formal analysis, Methodology, Writing - Review & Editing, Supervision, Funding acquisition.

Declaration of Competing Interest

The authors declare that they have no known competing financial interests or personal relationships that could have appeared to influence the work reported in this paper.

Data Availability

Data will be made available on request.

Acknowledgements

This work was supported by the Chinese National Science Foundation (Nos. 22075008, 21571010, and U0734002), the National Basic Research Programs of China (973 Program, Nos. 2014CB931800 and 2011CB935700), the Chinese Aeronautic Project (No. 2013ZF51069), and the 111 Project (No. B14009). This work was carried out with the support of the 1W1B X-ray absorption spectrum station beamline at the Beijing Synchrotron Radiation Facility.

Appendix A. Supporting information

Supplementary data associated with this article can be found in the online version at [doi:10.1016/j.apcatb.2023.122876](https://doi.org/10.1016/j.apcatb.2023.122876).

References

- [1] A. Manthiram, Y. Fu, S.-H. Chung, C. Zu, Y.-S. Su, Rechargeable lithium-sulfur batteries, *Chem. Rev.* 114 (2014) 11751–11787.
- [2] X. Ji, K.T. Lee, L.F. Nazar, A highly ordered nanostructured carbon-sulphur cathode for lithium-sulphur batteries, *Nat. Mater.* 8 (2009) 500–506.
- [3] Q. Pang, X. Liang, C.Y. Kwok, L.F. Nazar, Advances in lithium-sulfur batteries based on multifunctional cathodes and electrolytes, *Nat. Energy* 1 (2016) 16132.
- [4] L. Peng, Z. Wei, C. Wan, J. Li, Z. Chen, D. Zhu, D. Baumann, H. Liu, C.S. Allen, X. Xu, A.I. Kirkland, I. Shakir, Z. Almutairi, S. Tolbert, B. Dunn, Y. Huang, P. Sautet, X. Duan, A fundamental look at electrocatalytic sulfur reduction reaction, *Nat. Catal.* 3 (2020) 762–770.
- [5] Z. Shen, X. Jin, J. Tian, M. Li, Y. Yuan, S. Zhang, S. Fang, X. Fan, W. Xu, H. Lu, J. Lu, H. Zhang, Cation-doped ZnS catalysts for polysulfide conversion in lithium-sulfur batteries, *Nat. Catal.* 5 (2022) 555–563.
- [6] A. Manthiram, S.-H. Chung, C. Zu, Lithium-sulfur batteries: progress and prospects, *Adv. Mater.* 27 (2015) 1980–2006.
- [7] M. Zhao, B.-Q. Li, X.-Q. Zhang, J.-Q. Huang, Q. Zhang, A perspective toward practical lithium-sulfur batteries, *ACS Cent. Sci.* 6 (2020) 1095–1104.
- [8] Y. Li, S. Guo, Material design and structure optimization for rechargeable lithium-sulfur batteries, *Matter* 4 (2021) 1142–1188.
- [9] W. Sun, C. Liu, Y. Li, S. Luo, S. Liu, X. Hong, K. Xie, Y. Liu, X. Tan, C. Zheng, Rational construction of Fe₂N@C yolk-shell nanoboxes as multifunctional hosts for ultralong lithium-sulfur batteries, *ACS Nano* 13 (2019) 12137–12147.
- [10] D.-R. Deng, C. Li, J.-C. Weng, X.-H. Fan, Z.-J. Chen, G. Yang, Y. Li, Q.-H. Wu, M.-S. Zheng, Q.-F. Dong, Thin Nano Cages with Limited Hollow space for ultrahigh sulfur loading lithium-sulfur batteries, *ACS Appl. Mater. Interfaces* 14 (2022) 45414–45422.
- [11] W. Sun, S. Liu, Y. Li, D. Wang, Q. Guo, X. Hong, K. Xie, Z. Ma, C. Zheng, S. Xiong, Monodispersed FeS₂ electrocatalyst anchored to nitrogen-doped carbon host for lithium-sulfur batteries, *Adv. Funct. Mater.* 32 (2022), 2205471.
- [12] D.-R. Deng, X.-Y. Cui, X.-X. Fan, J.-Q. Zheng, X.-H. Fan, Q.-H. Wu, M.-S. Zheng, Q.-F. Dong, Integration of adsorption and catalytic active sites in cobalt iron oxide nanorods for an excellent performance Li-S battery with a wide temperature range, *Sustain. Energy Fuels* 5 (2021) 4284–4288.
- [13] D.-R. Deng, R.-M. Yuan, P.-K. Yu, F. Xue, X.-X. Fan, J. Lei, J.-L. Zhang, X.-D. Lin, Q.-H. Wu, J.-M. Fan, J.-K. Chang, W.-J. Hong, M.-S. Zheng, Q.-F. Dong, An enhanced electrode via coupling with a conducting molecule to extend interfacial reactions, *Adv. Energy Mater.* 11 (2021), 2101156.
- [14] D.-R. Deng, C.-D. Bai, F. Xue, J. Lei, P. Xu, M.-S. Zheng, Q.-F. Dong, Multifunctional Ion-Sieve Constructed by 2D Materials as an Interlayer for Li-S Batteries, *ACS Appl. Mater. Interfaces* 11 (2019) 11474–11480.
- [15] L. Fan, M. Li, X. Li, W. Xiao, Z. Chen, J. Lu, Interlayer material selection for lithium-sulfur batteries, *Joule* 3 (2019) 361–386.
- [16] S. Ji, Y. Chen, X. Wang, Z. Zhang, D. Wang, Y. Li, Chemical synthesis of single atomic site catalysts, *Chem. Rev.* 120 (2020) 11900–11955.
- [17] L. Liu, A. Corma, Metal catalysts for heterogeneous catalysis: from single atoms to nanoclusters and nanoparticles, *Chem. Rev.* 118 (2018) 4981–5079.
- [18] Z. Liang, J. Shen, X. Xu, F. Li, J. Liu, B. Yuan, Y. Yu, M. Zhu, Advances in the development of single-atom catalysts for high-energy-density lithium-sulfur batteries, *Adv. Mater.* 34 (2022), 2200102.
- [19] Z. Du, X. Chen, W. Hu, C. Chuang, S. Xie, A. Hu, W. Yan, X. Kong, X. Wu, H. Ji, L.-J. Wan, Cobalt in nitrogen-doped graphene as single-atom catalyst for high-sulfur content lithium-sulfur batteries, *J. Am. Chem. Soc.* 141 (2019) 3977–3985.
- [20] R. Zhang, B. Xue, Y. Tao, H. Zhao, Z. Zhang, X. Wang, X. Zhou, B. Jiang, Z. Yang, X. Yan, K. Fan, Edge-site engineering of defective Fe-N₄ nanozymes with boosted catalase-like performance for retinal vasculopathies, *Adv. Mater.* 34 (2022), 2205324.
- [21] G. Han, X. Zhang, W. Liu, Q. Zhang, Z. Wang, J. Cheng, T. Yao, L. Gu, C. Du, Y. Gao, G. Yin, Substrate strain tunes operando geometric distortion and oxygen reduction activity of CuN₂C₂ single-atom sites, *Nat. Commun.* 12 (2021) 6335.
- [22] D. Liu, X. Li, S. Chen, H. Yan, C. Wang, C. Wu, Y.A. Haleem, S. Duan, J. Lu, B. Ge, P. M. Ajayan, Y. Luo, J. Jiang, L. Song, Atomically dispersed platinum supported on curved carbon supports for efficient electrocatalytic hydrogen evolution, *Nat. Energy* 4 (2019) 512–518.
- [23] X. Wang, Y. Jia, X. Mao, D. Liu, W. He, J. Li, J. Liu, X. Yan, J. Chen, L. Song, A. Du, X. Yao, Edge-rich Fe-N₄ active sites in defective carbon for oxygen reduction catalysis, *Adv. Mater.* 32 (2020), 2000966.
- [24] C. Xia, Y. Qiu, Y. Xia, P. Zhu, G. King, X. Zhang, Z. Wu, J.Y. Kim, D.A. Cullen, D. Zheng, P. Li, M. Shakouri, E. Heredia, P. Cui, H.N. Alshareef, Y. Hu, H. Wang, General synthesis of single-atom catalysts with high metal loading using graphene quantum dots, *Nat. Chem.* 13 (2021) 887–894.
- [25] M. Yang, K. Wu, S. Sun, J. Duan, X. Liu, J. Cui, S. Liang, Y. Ren, Unprecedented relay catalysis of curved Fe₁-N₄ single-atom site for remarkably efficient ¹O₂ generation, *ACS Catal.* 13 (2023) 681–691.
- [26] J. Kim, S.-J. Kim, E. Jung, D.H. Mok, V.K. Paidi, J. Lee, H.S. Lee, Y. Jeoun, W. Ko, H. Shin, B.-H. Lee, S.-Y. Kim, H. Kim, J.H. Kim, S.-P. Cho, K.-S. Lee, S. Back, S.-H. Yu, Y.-E. Sung, T. Hyeon, Atomic structure modification of Fe-N-C catalysts via morphology engineering of graphene for enhanced conversion kinetics of lithium-sulfur batteries, *Adv. Funct. Mater.* 32 (2022), 2110857.
- [27] J. Feng, H. Gao, L. Zheng, Z. Chen, S. Zeng, C. Jiang, H. Dong, L. Liu, S. Zhang, X. Zhang, A. Mn-N₃, single-atom catalyst embedded in graphitic carbon nitride for efficient CO₂ electroreduction, *Nat. Commun.* 11 (2020) 4341.
- [28] E.S. Andreiadis, P.-A. Jacques, P.D. Tran, A. Leyris, M. Chavarot-Kerlidou, B. Jousset, M. Matheron, J. Pécaut, S. Palacin, M. Fontecave, V. Artero, Molecular engineering of a cobalt-based electrocatalytic nanomaterial for H₂ evolution under fully aqueous conditions, *Nat. Chem.* 5 (2013) 48–53.
- [29] Y. Wu, Z. Jiang, X. Lu, Y. Liang, H. Wang, Domino electroreduction of CO₂ to methanol on a molecular catalyst, *Nature* 575 (2019) 639–642.
- [30] H. Nara, T. Yokoshima, H. Mikuriya, S. Tsuda, T. Momma, T. Osaka, The potential for the creation of a high areal capacity lithium-sulfur battery using a metal foam current collector, *J. Electrochem. Soc.* 164 (2017) A5026–A5030.

- [31] G. Zhou, L. Li, C. Ma, S. Wang, Y. Shi, N. Koratkar, W. Ren, F. Li, H.-M. Cheng, A graphene foam electrode with high sulfur loading for flexible and high energy Li-S batteries, *Nano Energy* 11 (2015) 356–365.
- [32] D.J. Noelle, M. Wang, Y. Qiao, Improved safety and mechanical characterizations of thick lithium-ion battery electrodes structured with porous metal current collectors, *J. Power Sources* 399 (2018) 125–132.
- [33] Q. Wang, Q. Feng, Y. Lei, S. Tang, L. Xu, Y. Xiong, G. Fang, Y. Wang, P. Yang, J. Liu, W. Liu, X. Xiong, Quasi-solid-state Zn-air batteries with an atomically dispersed cobalt electrocatalyst and organohydrogel electrolyte, *Nat. Commun.* 13 (2022) 3689.
- [34] Y. Zhang, C. Kang, W. Zhao, Y. Song, J. Zhu, H. Huo, Y. Ma, C. Du, P. Zuo, S. Lou, G. Yin, d-p hybridization-induced “trapping-coupling-conversion” enables high-efficiency Nb single-atom catalysis for Li-S batteries, *J. Am. Chem. Soc.* 145 (2023) 1728–1739.
- [35] Y. Zhao, P.V. Kumar, X. Tan, X. Lu, X. Zhu, J. Jiang, J. Pan, S. Xi, H.Y. Yang, Z. Ma, T. Wan, D. Chu, W. Jiang, S.C. Smith, R. Amal, Z. Han, X. Lu, Modulating Pt-O-Pt atomic clusters with isolated cobalt atoms for enhanced hydrogen evolution catalysis, *Nat. Commun.* 13 (2022) 2430.
- [36] L. Zhang, D. Liu, Z. Muhammad, F. Wan, W. Xie, Y. Wang, L. Song, Z. Niu, J. Chen, Single nickel atoms on nitrogen-doped graphene enabling enhanced kinetics of lithium-sulfur Batteries, *Adv. Mater.* 31 (2019), 1903955.
- [37] L.-N. Song, W. Zhang, Y. Wang, X. Ge, L.-C. Zou, H.-F. Wang, X.-X. Wang, Q.-C. Liu, F. Li, J.-J. Xu, Tuning lithium-peroxide formation and decomposition routes with single-atom catalysts for lithium-oxygen batteries, *Nat. Commun.* 11 (2020) 2191.
- [38] Z. Zhang, X. Zhao, S. Xi, L. Zhang, Z. Chen, Z. Zeng, M. Huang, H. Yang, B. Liu, S. J. Pennycook, P. Chen, Atomically dispersed cobalt trifunctional electrocatalysts with tailored coordination environment for flexible rechargeable Zn-air battery and self-driven water splitting, *Adv. Energy Mater.* 10 (2020), 2002896.
- [39] Y. Zhang, J. Liu, J. Wang, Y. Zhao, D. Luo, A. Yu, X. Wang, Z. Chen, Engineering oversaturated Fe-N₅ multifunctional catalytic sites for durable lithium-sulfur Batteries, *Angew. Chem. Int. Ed.* 60 (2021) 26622–26629.
- [40] R. Yan, Z. Zhao, M. Cheng, Z. Yang, C. Cheng, X. Liu, B. Yin, S. Li, Origin and acceleration of insoluble Li₂S₂-Li₂S reduction catalysis in ferromagnetic atoms-based lithium-sulfur battery cathodes, *Angew. Chem. Int. Ed.* 62 (2023), e202215414.
- [41] A. Zitolo, V. Goellner, V. Armel, M.-T. Sougrati, T. Mineva, L. Stievano, E. Fonda, F. Jaouen, Identification of catalytic sites for oxygen reduction in iron- and nitrogen-doped graphene materials, *Nat. Mater.* 14 (2015) 937–942.
- [42] Z. Shen, M. Cao, Z. Zhang, J. Pu, C. Zhong, J. Li, H. Ma, F. Li, J. Zhu, F. Pan, H. Zhang, Efficient Ni₂Co₄P₃ nanowires catalysts enhance ultrahigh-loading lithium-sulfur conversion in a microreactor-like battery, *Adv. Funct. Mater.* 30 (3) (2020), 1906661.
- [43] F. Zhang, Y. Wang, W. Guo, S. Rao, P. Mao, Synthesis of Sn-MnO@nitrogen-doped carbon yolk-shelled three-dimensional interconnected networks as a high-performance anode material for lithium-ion batteries, *Chem. Eng. J.* 360 (2019) 1509–1516.
- [44] T. Huang, Y. Sun, J. Wu, Z. Shi, Y. Ding, M. Wang, C. Su, Y.-Y. Li, J. Sun, Altering local chemistry of single-atom coordination boosts bidirectional polysulfide conversion of Li-S batteries, *Adv. Funct. Mater.* 32 (2022), 2203902.
- [45] S. He, J. Yang, S. Liu, X. Wang, X. Che, M. Wang, J. Qiu, Asymmetric N-coordinated iron single-atom catalysts supported on graphitic carbon for polysulfide conversion in lithium-sulfur batteries, *Chem. Eng. J.* 454 (2023), 140202.
- [46] C. Wang, H. Song, C. Yu, Z. Ullah, Z. Guan, R. Chu, Y. Zhang, L. Zhao, Q. Li, L. Liu, Iron single-atom catalyst anchored on nitrogen-rich MOF-derived carbon nanocage to accelerate polysulfide redox conversion for lithium sulfur batteries, *J. Mater. Chem. A* 8 (2020) 3421–3430.
- [47] Y. Jia, W. Gong, X. Fan, S. Chen, X. Meng, Y. Meng, J. Zhou, Y. Cao, S. Hong, L. Zheng, Z. Wang, C.W. Bielawski, J. Geng, Coaxially grafting conjugated microporous polymers containing single-atom cobalt catalysts to carbon nanotubes enhances sulfur cathode reaction kinetics, *Chem. Eng. J.* 444 (2022), 136546.
- [48] Y. Li, Y. Zeng, Y. Chen, D. Luan, S. Gao, X.W. Lou, Mesoporous N-rich carbon with single-Ni atoms as a multifunctional sulfur host for Li-S batteries, *Angew. Chem. Int. Ed.* 61 (2022), e202212680.
- [49] C. Dong, C. Zhou, Y. Li, Y. Yu, T. Zhao, G. Zhang, X. Chen, K. Yan, L. Mai, X. Xu, Ni single atoms on MoS₂ nanosheets enabling enhanced kinetics of Li-S batteries, *Small* 19 (2023), 2205855.
- [50] L. Zhang, J. Bi, T. Liu, X. Chu, H. Lv, D. Mu, B. Wu, F. Wu, TiN/TiC heterostructures embedded with single tungsten atoms enhance polysulfide entrapment and conversion for high-capacity lithium-sulfur battery applications, *Energy Storage Mater.* 54 (2023) 410–420.
- [51] S. Yu, Y. Sun, L. Song, X. Cao, L. Chen, X. An, X. Liu, W. Cai, T. Yao, Y. Song, W. Zhang, Vanadium atom modulated electrocatalyst for accelerated Li-S chemistry, *Nano Energy* 89 (2021), 106414.
- [52] D. Guo, X. Zhang, M. Liu, Z. Yu, Xa Chen, B. Yang, Z. Zhou, S. Wang, Single Mo-N₄ atomic sites anchored on N-doped carbon nanoflowers as sulfur host with multiple immobilization and catalytic effects for high-performance lithium-sulfur batteries, *Adv. Funct. Mater.* 32 (2022), 2204458.
- [53] D. Yang, Z. Liang, P. Tang, C. Zhang, M. Tang, Q. Li, J.J. Biendicho, J. Li, M. Heggen, R.E. Dunin-Borkowski, M. Xu, J. Llorca, J. Arbiol, J.R. Morante, S.-L. Chou, A. Cabot, A high conductivity 1D π - π conjugated metal-organic framework with efficient polysulfide trapping-diffusion-catalysis in lithium-sulfur batteries, *Adv. Mater.* 34 (2022), 2108835.
- [54] D. Wang, K. Ma, J. Hao, W. Zhang, C. Wang, C. Xu, H. Shi, Z. Ji, X. Yan, Y. Gu, Multifunction Co-N_x species to manipulate polysulfides conversion kinetics toward highly efficient lithium-sulfur batteries, *Nano Energy* 89 (2021), 106426.
- [55] X. Zhang, T. Yang, Y. Zhang, X. Wang, J. Wang, Y. Li, A. Yu, X. Wang, Z. Chen, Single zinc atom aggregates: synergetic interaction to boost fast polysulfide conversion in lithium-sulfur batteries, *Adv. Mater.* 35 (2023), 2208470.
- [56] Z. Han, S. Zhao, J. Xiao, X. Zhong, J. Sheng, W. Lv, Q. Zhang, G. Zhou, H.-M. Cheng, Engineering d-p orbital hybridization in single-atom metal-embedded three-dimensional electrodes for Li-S batteries, *Adv. Mater.* 33 (2021), 2105947.
- [57] P. Wang, B. Xi, Z. Zhang, M. Huang, J. Feng, S. Xiong, Atomic tungsten on graphene with unique coordination enabling kinetically boosted lithium-sulfur batteries, *Angew. Chem. Int. Ed.* 60 (2021) 15563–15571.
- [58] X. Yao, C. Guo, C. Song, M. Lu, Y. Zhang, J. Zhou, H.-M. Ding, Y. Chen, S.-L. Li, Y.-Q. Lan, In situ interweaved high sulfur loading Li-S cathode by catalytically active metalloporphyrin based organic polymer binders, *Adv. Mater.* 35 (2023), 2208846.
- [59] X. Sun, Y. Qiu, B. Jiang, Z. Chen, C. Zhao, H. Zhou, L. Yang, L. Fan, Y. Zhang, N. Zhang, Isolated Fe-Co heteronuclear diatomic sites as efficient bifunctional catalysts for high-performance lithium-sulfur batteries, *Nat. Commun.* 14 (2023) 291.